

Accepted Manuscript

The formation and chronology of the PAT 91501 impact-melt L-chondrite with vesicle-metal-sulfide assemblages

G.K. Benedix, R.A. Ketcham, L. Wilson, T.J. McCoy, D.D. Bogard, D.H. Garrison, G.F. Herzog, S. Xue, J. Klein, R. Middleton

PII: S0016-7037(08)00082-3
DOI: [10.1016/j.gca.2008.02.010](https://doi.org/10.1016/j.gca.2008.02.010)
Reference: GCA 5552

To appear in: *Geochimica et Cosmochimica Acta*

Received Date: 31 May 2007
Accepted Date: 11 February 2008

Please cite this article as: Benedix, G.K., Ketcham, R.A., Wilson, L., McCoy, T.J., Bogard, D.D., Garrison, D.H., Herzog, G.F., Xue, S., Klein, J., Middleton, R., The formation and chronology of the PAT 91501 impact-melt L-chondrite with vesicle-metal-sulfide assemblages, *Geochimica et Cosmochimica Acta* (2008), doi: [10.1016/j.gca.2008.02.010](https://doi.org/10.1016/j.gca.2008.02.010)

This is a PDF file of an unedited manuscript that has been accepted for publication. As a service to our customers we are providing this early version of the manuscript. The manuscript will undergo copyediting, typesetting, and review of the resulting proof before it is published in its final form. Please note that during the production process errors may be discovered which could affect the content, and all legal disclaimers that apply to the journal pertain.



1
2
3
4
5
6
7
8
9
10 **The formation and chronology of the PAT 91501 impact-melt L-chondrite with**
11 **vesicle-metal-sulfide assemblages**
12
13
14
15

16 G.K. Benedix¹, R.A. Ketcham², L. Wilson³, T.J. McCoy⁴, D.D. Bogard⁵, D.H. Garrison⁶,
17 G.F. Herzog⁷, S. Xue⁷, J. Klein⁸, and R. Middleton^{8,*}
18
19
20
21
22

23 ¹Impact and Astromaterials Research Centre (IARC)/Department of Mineralogy, The
24 Natural History Museum, Cromwell Road, London, SW7 5BD UK
25 (g.benedix@nhm.ac.uk)

26 ²Dept. of Geological Sciences, Jackson School of Geosciences, Univ. of Texas at Austin,
27 Austin, TX 78712 USA

28 ³Environmental Sci. Dept., Lancaster Univ., Lancaster LA1 4YQ UK.

29 ⁴Dept. of Mineral Sciences, National Museum of Natural History, Smithsonian
30 Institution, Washington, DC 20560-0119 USA

31 ⁵ARES, NASA-JSC, Houston TX 77058

32 ⁶ESCG/Barrios Technology, Houston, TX 77058

33 ⁷Rutgers Univ., Piscataway, NJ 08854-8087

34 ⁸Univ. Pennsylvania, Philadelphia, PA 19104.
35
36
37
38

39 Submitted to *Geochimica et Cosmochimica Acta* May 2007

40 Revision submitted in February 2008

41 **Deceased*

42 **Abstract** – The L chondrite Patuxent Range (PAT) 91501 is an 8.5-kg unshocked,
43 homogeneous, igneous-textured impact melt that cooled slowly compared to other
44 meteoritic impact melts in a crater floor melt sheet or sub-crater dike (Mittlefehldt and
45 Lindstrom, 2001). We conducted mineralogical and tomographic studies of previously
46 unstudied mm- to cm-sized metal-sulfide-vesicle assemblages and chronologic studies of
47 the silicate host. Metal-sulfide clasts constitute about 1 vol.%, comprise zoned taenite,
48 troilite, and pentlandite, and exhibit a consistent orientation between metal and sulfide
49 and of metal-sulfide contacts. Vesicles make up ~2 vol.% and exhibit a similar
50 orientation of long axes. ^{39}Ar - ^{40}Ar measurements probably date the time of impact at
51 4.461 ± 0.008 Gyr B.P. Cosmogenic noble gases and ^{10}Be and ^{26}Al activities suggest a
52 pre-atmospheric radius of 40-60 cm and a cosmic ray exposure age of 25-29 Myr, similar
53 to ages of a cluster of L chondrites. PAT 91501 dates the oldest known impact on the L
54 chondrite parent body. The dominant vesicle-forming gas was S_2 (~15-20 ppm), which
55 formed in equilibrium with impact-melted sulfides. The meteorite formed in an impact
56 melt dike beneath a crater, as did other impact melted L chondrites, such as Chico.
57 Cooling and solidification occurred over ~2 hours. During this time, ~90% of metal and
58 sulfide segregated from the local melt. Remaining metal and sulfide grains oriented
59 themselves in the local gravitational field, a feature nearly unique among meteorites.
60 Many of these metal-sulfide grains adhered to vesicles to form aggregates that may have
61 been close to neutrally buoyant. These aggregates would have been carried upward with
62 the residual melt, inhibiting further buoyancy-driven segregation. Although similar
63 processes operated individually in other chondritic impact melts, their interaction
64 produced the unique assemblage observed in PAT 91501.

65

1. INTRODUCTION

66

67

68

69

70

71

72

73

74

75

76

77

78

79

80

81

82

83

84

85

86

87

Impact is one of three fundamental processes that, along with accretion and differentiation, formed and modified asteroid bodies. From nebular accretion through to modern times, impact has left its traces in the ubiquitous cratered surfaces, distorted shapes, and telltale signs of shocked minerals and melts recorded in meteorites. Radiometric chronology reveals impact disturbance or resetting of isotopic systems on several meteorite parent bodies over a wide range in time, but mostly in the periods of 3.5-4.0 Gyr and <1 Gyr ago (Bogard, 1995). Cosmic ray exposure ages of stony meteorites often date the time of impact-induced ejection from their parent objects and are essentially all less than 0.1 Gyr (Herzog, 2005). Despite abundant evidence, however, our knowledge of the physical processes and the timing of impact on asteroidal bodies remains incomplete. While we have systematic sampling from many well-documented impact craters on Earth to serve as our guide to interpreting impact phenomena on other planets, we have only sparse and random sampling of asteroidal impact craters. Further, our knowledge of chronology is limited because the samples we do have may not accurately reflect the impact flux throughout the history of the Solar System. Examples within meteorites of relatively large impacts during the first ~0.2 Gyr of planetary history, when some parent objects were still experiencing metamorphism, are particularly rare. Continuing study of impact-derived meteorites can help fill these gaps in our knowledge.

Melt veined meteorites, impact melt breccias, and impact melts are not uncommon among the known ordinary chondrite population and have been studied extensively (Rubin, 1985; Stöffler et al., 1991). In particular, considerable effort has

88 focused on relating these meteorites to the physical setting of their formation, starting
89 with the location of their melt. Melt can form on the floor and walls during formation of a
90 crater or in subsurface dikes that may extend below the crater into the country rock. Each
91 of these settings provides a unique physical and thermal environment for the
92 incorporation of clastic material and cooling history. In the case of the floor melts, they
93 will be exposed to space prior to being covered by falling debris or wall collapse. The
94 dike melts will be shielded from space exposure and allow the melt to remain clast-free.

95 Impact rates were much higher in the early history of the solar system (Hartmann
96 et al., 2000), but those impacts are probably recorded in the asteroid belt by the
97 population of small bodies produced by the break-up of larger precursor asteroids.
98 Impact craters observed on asteroids today are more recent events, consistent with the
99 fact that most strong impact events in chondrites occurred within the past 1 Gyr, as
100 determined by Ar-Ar radiometric dating (Bogard, 1995, and references therein). For
101 example, many L-chondrites show Ar-Ar impact heating ages clustering near 0.5 Gyr,
102 perhaps dating the time of disruption of the parent body (Haack et al., 1996;
103 Korochantseva et al., 2007). Interestingly, chronological evidence for collisional events
104 very early in asteroid history is sparse.

105 This paper presents a multidisciplinary study of PAT 91501, a vesicular, impact
106 melted L chondrite (Score and Lindstrom, 1992). Vesicles have been reported in only
107 two other ordinary chondrite impact melts: Shaw (Taylor et al., 1979) and Cat Mountain
108 (Kring et al., 1996). Although these meteorites are chemically and petrologically well-
109 characterized (Harvey and Roeder, 1994, Mittlefehldt and Lindstrom, 2001), no study has
110 addressed the implications of the presence of vesicles in impact melt rocks. Our

111 objectives were to document the meteorite's impact and cosmic ray exposure history and
112 to understand the genesis of the unusual vesicular nature of this meteorite.

113

2. PREVIOUS WORK

114 The petrology of the silicate portion of PAT 91501 is reported by Harvey and
115 Roedder (1994) and Mittlefehldt and Lindstrom (2001). We briefly review these studies
116 here. PAT 91501 is an unshocked, homogeneous, igneous-textured rock of broadly L
117 chondrite mineralogy and chemistry. Major element mineral chemistries were shown to
118 be consistent with those of L-type chondrites; the minor element chemistry of olivine and
119 low-Ca pyroxene, on the other hand, is consistent with melting (Mittlefehldt and
120 Lindstrom, 2001); depletions of Zn and Br and sequestration of siderophile and
121 chalcophile elements into the large, heterogeneously-distributed metal-sulfide aggregates
122 were observed (Mittlefehldt and Lindstrom, 2001). Relic material includes rare
123 chondrules, as well as opaque-inclusion-rich olivine and some low-Ca pyroxene grains
124 that constitute ~10 vol.% of the meteorite, but distinct unmelted clasts, commonly found
125 in impact melt breccias, are absent. Mittlefehldt and Lindstrom (2001) concluded that
126 PAT 91501 is an impact melt of an L chondrite that crystallized at a cooling rate slower
127 than that typical for impacts melts and likely formed in a melt sheet on the crater floor or
128 in a sub-crater melt dike.

129

3. SAMPLES AND ANALYTICAL TECHNIQUES

130 Patuxent Range (PAT) 91501 was recovered in Antarctica during the 1991-1992
131 collecting season. Numerous large and small pieces, totaling more than 8.5 kg, were
132 collected. Their relative positions in the meteoroid are unknown. In the same locale, two
133 small metal-sulfide nodules (PAT 91516 and 91528; Clarke, 1994) were recovered. As

134 discussed below, these meteorites are petrologically identical to metal-sulfide nodules
135 from PAT 95101.

136 PAT 91501 was originally classified as an L7 chondrite (Score and Lindstrom,
137 1992) based on textural features, mineral chemistry and oxygen isotopic composition,
138 although it was noted that it was similar in many respects to the Shaw L chondrite impact
139 melt. On further investigation (Harvey and Roedder, 1994; Mittlefehldt and Lindstrom,
140 2001), it was determined to be a near-total impact melt of an L chondrite.

141 One of the most striking features of PAT 91501 is the mm- to cm-sized vesicles
142 seen on cut surfaces of the sample (Fig. 1), as originally noted by Marlow et al. (1992).
143 We focused on PAT 91501 because it contains large vesicles that are visible in hand
144 sample (Fig. 1), there is abundant material, and it has been described as a total impact
145 melt (Mittlefehldt and Lindstrom, 2001). Visual inspection of PAT 91501 ,50 (2814.3 g)
146 and ,78 (127.6 g) show clastless, light colored surfaces with cm-sized vesicles and
147 metal/troilite aggregates.

148 **3.1 Petrology**

149 All thin sections of PAT 91501 (,26; ,27; ,28; ,95; and ,111) available at the
150 Smithsonian National Museum Natural History, as well as sections of PAT 91516 and
151 PAT 91528, were examined in both reflected and transmitted light with an optical
152 microscope. Metal and troilite compositions were analyzed using a JEOL JXA 8900R
153 electron microprobe at the Smithsonian. Analytical conditions were 20kV and 20nA.
154 Well-known standards were used and analyses were corrected using a manufacturer
155 supplied ZAF correction routine. Sulfur isotopes were analyzed using the 6f ion

156 microprobe at the Carnegie Institution of Washington utilizing Canyon Diablo troilite as
157 the standard.

158 The two hand samples described above (,50 and ,78) were imaged at the High
159 Resolution X-ray Computed Tomography facility at the University of Texas at Austin
160 (UTCT), which is described in detail by Ketcham and Carlson (2001). The focus of our
161 work was to determine the distribution of vesicles, metal, and sulfide, which are easily
162 distinguished based on their large density contrast from the silicate matrix. Sample PAT
163 91501 ,50 was scanned using the high-energy subsystem, with the X-ray energy set at
164 420 kV and 4.7 mA, with a focal spot size of 1.8 mm. The samples were scanned in air
165 and, to reduce scan artifacts, the beam was pre-filtered with 1.58 mm of brass. Each slice
166 was reconstructed from 1800 views, with an acquisition time of 128 ms per view. A total
167 of 141 (1024x1024) slices were acquired with a thickness and spacing of 0.5 mm,
168 imaging a 196 mm field of view. The final scan images were post-processed for ring
169 artifact removal. Sample PAT 91501,78 was imaged using the microfocal subsystem,
170 with X-rays at 180 kV and 0.25 mA, and a focal spot size of approximately 0.05 mm.
171 The sample was sealed and placed in a cylinder and surrounded by water, which was used
172 as a wedge calibration to reduce scan artifacts. Data for 31 slice images were acquired
173 during each rotation of the sample; over each rotation, 1000 views were acquired with an
174 acquisition time of 267 ms per view. A total of 927 (1024x1024) slices at 0.0726 mm
175 intervals, each showing a 67 mm field of view, were acquired. Scans were reconstructed
176 using a software correction to further reduce beam-hardening artifacts. Animations,
177 including flipbooks for the 2D computed tomography scans and 3D rotational renderings
178 are available in the electronic annex.

179 Measurements of vesicles and metal/troilite particles from the CT data volume
180 were made using Blob3D software (Ketcham, 2005), and visualizations were made using
181 Amira® version 3.1.

182 **3.2 Chronology (^{39}Ar - ^{40}Ar ages and cosmic-ray exposure ages)**

183 A 48-mg whole rock sample of PAT91501 ,109 was irradiated with fast neutrons,
184 along with multiple samples of the NL-25 hornblende age standard. This irradiation
185 converted a portion of the ^{39}K into ^{39}Ar , and the $^{40}\text{Ar}/^{39}\text{Ar}$ ratio yields the K-Ar age. The
186 irradiation constant (J-value) was $0.02521_0 \pm 0.00012_5$. Ar was released from PAT 91501
187 in 34 stepwise temperature extractions and its isotopic composition was measured on a
188 mass spectrometer. Experimental details are given in Bogard et al. (1995). Two
189 unirradiated whole rock samples of PAT 91501, taken from different locations in the
190 meteorite (see below), were degassed in either two or four stepwise temperature
191 extractions and the He, Ne, and Ar released were analyzed on a mass spectrometer. All
192 noble gas analyses were made at NASA-JSC.

193 We analyzed chips from four different specimens (subsamples 34, 38, 40, and 42)
194 of PAT 91501 for cosmogenic radionuclides. Sample ,34 was located adjacent to sample
195 ,106, which was analyzed for noble gases. Using facilities at Rutgers, the four specimens
196 were ground and weighed. After addition of Al and Be carriers, the powders were
197 dissolved in strong mineral acids. Beryllium and aluminum were separated by ion
198 exchange, precipitated as the hydroxides, and ignited to the oxides as described by Vogt
199 and Herpers (1988). The activities of ^{10}Be and ^{26}Al were measured by accelerator mass
200 spectrometry at the University of Pennsylvania as described by Middleton and Klein

201 (1986) and Middleton et al. (1983) (Table 1). As the ^{10}Be activity of sample ,40 was
202 unaccountably low and inconsistent with the ^{26}Al activity, we do not report it.

203

204

4. RESULTS

205 We report our analyses of the metal-sulfide-vesicle assemblages, based on both
206 microscopic examination and computed tomography, and the results of the chronological
207 analyses for both ^{39}Ar - ^{40}Ar and cosmogenic noble gases and radionuclides.

208 4.1 Petrography of metal-sulfide assemblages

209 PAT 91501 contains both vesicles and rounded metal-sulfide nodules that reach 1
210 cm in diameter. Previous studies have focused primarily on the silicate portion (Harvey
211 and Roedder, 1994; Mittlefehldt and Lindstrom, 2001), with neither study reporting
212 detailed examination of a metal-sulfide nodule in thin section. As we discuss later,
213 metal-sulfide nodules are rare, with less than 1 per cm^3 . Apart from a single chemical
214 analysis of troilite reported by Mittlefehldt and Lindstrom (2001), they have not been
215 studied .

216 We examined a 5-mm-diameter metal-sulfide nodule adjacent to a 5-mm-diameter
217 vesicle in subsample ,111. This nodule consists of a core of Fe,Ni metal (2 by 3.5 mm)
218 rimmed by sulfide, with the two phases exhibiting numerous mutual protrusions into each
219 other. The sulfide is dominantly troilite, although minor (<1 vol.%) pentlandite
220 ($(\text{Fe}_{6.15}\text{Ni}_{2.62}\text{Co}_{0.10})_{=8.88}\text{S}_8$) is observed at troilite-metal, troilite-silicate and troilite-vesicle
221 boundaries. Schreibersite rims are often found at the border between metal and
222 troilite/pentlandite. The S isotopic composition of pentlandite (3 analyses yield $\delta^{34}\text{S}$ of
223 0.5-1.9‰) and troilite (7 analyses yield $\delta^{34}\text{S}$ of 0.4-1.2‰) are essentially identical. No

224 polycrystallinity or twinning is observed in the troilite, confirming the observation of
225 Mittlefehldt and Lindstrom (2001) that PAT 91501 experienced minimal secondary shock
226 after its crystallization. The metal is composed of two domains (Fig. 2a). Rimming each
227 domain is a 50 μm thick region of high-Ni (up to 45 wt.%; Fig. 2b) taenite that is
228 relatively inclusion free. Adjacent to this, Ni decreases systematically from ~40 wt.% to
229 ~20 wt.% and this zoned metal often contains 10-30 μm troilite and 1-5 μm schreibersite
230 inclusions. The center of the largest domain, which appears to have been bisected, is
231 martensitic, with irregular Ni concentrations of 20-25 wt.%, and contains troilite and
232 schreibersite inclusions that can reach tens of microns.

233 While metal-sulfide nodules from PAT 91501 have not been previously described,
234 the published descriptions (Clarke, 1994) for the small iron meteorites PAT 91516 (1.58
235 g) and PAT 91528 (3.34 g) are essentially identical to that given here for PAT 91501.
236 The only substantive difference is that Clarke observed a larger number of metal
237 domains, particularly in PAT 91516, and these were often separated by sinuous troilite.

238 **4.2 Computed Tomography**

239 We used computed tomography (CT) to survey the distribution of vesicles, metal
240 and sulfide in two samples of PAT 91501 (see electronic annex EA-2 and EA-4). Figure
241 3 is a single frame of a 3 dimensional, rotational visualization (see electronic annex EA-
242 1) made from the CT scan of PAT 91501 ,50, in which vesicles and metal-sulfide
243 intergrowths are highlighted. In this sample, 5085 vesicles were measured, which
244 comprise ~2 volume percent of the sample. The sizes of the vesicles range in diameter
245 from 0.6 to 14 μm . In contrast, analysis of PAT 91501 ,78 yielded 36685 vesicles
246 ranging in size from 0.2 to ~6 μm in diameter. The difference in the numbers and the size

247 range of vesicles is due to the fact that the smaller sample was scanned at a much higher
248 resolution. In both samples, tiny vesicles (<1mm diameter) dominate the population.
249 Vesicles in both samples are homogeneously distributed and have a median aspect ratio of
250 1.4, indicating moderate elongation.

251 The CT scans revealed the existence and distribution of several large metal-
252 sulfide intergrowths (Fig. 3). Together, metal and sulfide represent less than 1 volume
253 percent of the sample. We measured 255 and 142 metal grains in sample ,50 and ,78,
254 respectively. Metal ranges in size from 0.7 to 8.6 mm in the larger sample and comprises
255 0.27 vol%, while in the smaller sample metal ranges from 0.1 to 3.8 mm and represents
256 0.35 vol%; as with the vesicles, the higher-resolution scan of the smaller sample
257 permitted us to measure particles too small to be resolved in the scan of the larger
258 specimen. Sulfide is more abundant than metal in both samples and occupies
259 approximately twice the volume as metal. Sulfide accounts for 0.4 vol% in the larger
260 sample (,50) and for 0.56 vol% in the smaller sample. We measured 404 sulfide grains in
261 sample ,50 and 540 grains in sample ,78. Sulfide is overall larger than metal and ranges
262 from 0.6 to 12.7mm in ,50 and from 0.2 to 4.7mm in ,78. As with vesicles, tiny grains (<
263 1mm) comprise the mode of both the metal and sulfide size distributions (see flipbooks
264 and 3D renderings in supplemental data).

265 PAT 91501 (,50) contains 169 grains in which metal and sulfide are in contact.
266 These particles were noted by earlier workers (Score and Lindstrom, 1992; Mittlefehldt
267 and Lindstrom, 2001) and attributed to formation as immiscible melts prior to silicate
268 crystallization. Interestingly, these particles exhibit a consistent orientation of the metal
269 and sulfide relative to each other and to the meteorite as a whole. Figure 4a is a stereo

270 plot of the normals to the planes defined by the contact between metal and sulfide with
271 the size of the each circle proportional to the area of the contact. Although some scatter
272 is observed in this plot, particularly for smaller metal-sulfide pairs, the majority of larger
273 particles defines a tight cluster trending 255° and plunging 45° ; note that these
274 orientations are with respect to the scan data, and are not geographical.

275 The CT scans also document the relationship between vesicles, metal, and sulfide.
276 Larger vesicles appear to have metal-sulfide intergrowths associated with them. In the
277 CT scan of the larger sample of PAT 91501, we found 18 instances where vesicles are in
278 contact with metal only, sulfide only or metal-sulfide intergrowths. In the higher
279 resolution CT scan of PAT 91501, 78, there are nearly 200 vesicles in contact with metal,
280 sulfide or metal-sulfide. The vast majority of the largest vesicles are in contact with
281 metal and/or sulfide.

282 The elongation of vesicles allows us to examine their orientation as well. Fig. 4b
283 is a stereo plot of the orientations of the vesicle long axes from the main mass of PAT
284 91501 (,50) with the circle areas proportional to vesicle volume. Again, considerable
285 scatter is observed, particularly among the smaller vesicles. However, the larger vesicles
286 define a distinct cluster trending 300° and plunging 40° , with the main outlier attributable
287 to contact with an irregular metal-sulfide mass. This cluster is offset $\sim 33^\circ$ from the
288 orientation defined by the normals to the metal-sulfide contacts.

289 **4.3 Ar-Ar Age**

290 The PAT 91501 Ar-Ar age spectrum (Fig. 5) appears complex but can be
291 interpreted to yield a reliable age. The rate of release of ^{39}Ar and changes in the K/Ca
292 ratio and the Ar-Ar age as a function of extraction temperature all suggest that ^{39}Ar is

293 contained in three distinct diffusion domains— 0-17%, 17-80%, and 80-100% ^{39}Ar release
294 (Fig 5). The ^{39}Ar release data can be modeled by standard diffusion theory in terms of
295 the parameter D/a^2 , where D is the diffusion coefficient and a is the average diffusion
296 length for Ar in the degassing grains. On an Arrhenius plot (argon released vs. $1/T$; not
297 shown), data for these three domains give separate linear trends, each one characterized
298 by a different value of D/a^2 . Above 80% ^{39}Ar release, the observed decreases in age and
299 K/Ca are interpreted to represent release of excess ^{39}Ar recoiled during irradiation into
300 the surfaces of pyroxene grains. Below ~17% ^{39}Ar release, the higher ages are
301 interpreted to represent loss of recoiled ^{39}Ar from surfaces of grains possessing a
302 relatively larger K/Ca ratio. Between ~19% and 80% of the ^{39}Ar release, the K/Ca ratio
303 is relatively constant and the Ar-Ar ages describe a plateau. Ten extractions releasing 19-
304 78% of the ^{39}Ar define an age of 4.463 ± 0.009 Gyr, where the age uncertainty is
305 approximately one-sigma and includes the uncertainty in the irradiation constant, J .
306 Seven extractions releasing 30-78% of the ^{39}Ar give an age of 4.461 ± 0.008 Gyr. To
307 examine these data in an isochron plot, we adopted the cosmogenic ^{38}Ar concentration
308 given below and used the measured $^{37}\text{Ar}/^{36}\text{Ar}$ ratios for each extraction to apportion the
309 measured ^{36}Ar into trapped and cosmogenic components. An isochron plot of $^{40}\text{Ar}/^{36}\text{Ar}$
310 versus $^{39}\text{Ar}/^{36}\text{Ar}$, using trapped ^{36}Ar , is highly linear ($R^2=0.9995$) and its slope yields an
311 age of 4.466 ± 0.0012 Myr, in agreement with the plateau age. The isochron intercept
312 value of $^{40}\text{Ar}/^{36}\text{Ar} = -79 \pm 56$ suggests all ^{40}Ar released in these extractions is radiogenic.
313 The total age summed across all extractions is 4.442 Gyr and suggests that little to no
314 ^{40}Ar was lost from the sample by diffusion over geologic time.

315 Although, we conclude that impact resetting of the K-Ar age in PAT91501
316 occurred 4.46 \pm 0.01 Gyr ago, several unshocked L and H chondrites show Ar-Ar ages
317 across a wide range of ~4.52-4.44 Gyr, presumably as a result of extended parent body
318 metamorphism (Turner et al., 1978; Pellas & Fiéni, 1988). Therefore, we cannot exclude
319 the possibility that the 4.46 Gyr Ar-Ar age of PAT91501 dates this L-chondrite
320 metamorphism and that the impact event occurred earlier.

321 **4.4 Cosmogenic Noble Gases and Radionuclides.**

322 PAT 91501 ,109 (33.4 mg) was heated in two temperature steps and sample ,106
323 (50.0 mg) was heated in four steps (Table 1). In both samples approximately half of the
324 ^3He was released at 500°C. In sample ,106 the peak of the Ne release occurred at 900-
325 1200 °C, and the peak of the ^{38}Ar release occurred at 1200 °C. Measured ^3He is entirely
326 cosmogenic. The summed $^{20}\text{Ne}/^{22}\text{Ne}$ ratios of 0.845-0.847 indicate that measured Ne is
327 also entirely cosmogenic. Consequently we summed concentrations for each Ne isotope
328 across all extractions to obtain total cosmogenic abundances. Measured $^{36}\text{Ar}/^{38}\text{Ar}$ ratios
329 varied over 0.72-1.75 and indicate the release of trapped Ar, which is mostly adsorbed
330 atmospheric Ar, particularly at lower extraction temperatures. We assumed $^{36}\text{Ar}/^{38}\text{Ar}$
331 ratios of 5.32 for trapped Ar and 0.67 for cosmogenic Ar and calculated the abundances
332 of cosmogenic ^{38}Ar for each extraction. The $^{38}\text{Ar}_{\text{cos}}$ abundances were then summed
333 across each extraction to obtain the total abundance of $^{38}\text{Ar}_{\text{cos}}$. From analyses of He, Ne,
334 and Ar delivered from a standard gas pipette, we estimate the uncertainty in these
335 abundances as $\sim\pm 10\%$.

336 Cosmogenic abundances and $^{22}\text{Ne}/^{21}\text{Ne}$ ratios for the two PAT samples are given
337 in Table 2. Cosmogenic abundances of ^3He , ^{21}Ne , and ^{38}Ar in the two samples agree with

338 each other within their individual uncertainties of $\pm 0\%$. The measured $^{20}\text{Ne}/^{21}\text{Ne}$ ratios
339 for ,109 and ,106 are identical at 0.847 ± 0.005 and 0.845 ± 0.015 . The measured $^{22}\text{Ne}/^{21}\text{Ne}$
340 ratios of 1.084 ± 0.003 and 1.097 ± 0.003 differ slightly, which probably reflects a shielding
341 difference. A plot of $^3\text{He}/^{21}\text{Ne}$ versus $^{22}\text{Ne}/^{21}\text{Ne}$ defines a shielding trend for many
342 chondrites (Eberhardt et al., 1966). Sample ,109 plots on this shielding trend, but sample
343 ,106 plots slightly above the trend, as a consequence of its lower ^{21}Ne concentration.
344 This observation may imply that in our ,106 sample the concentration of Mg, the main
345 target for $^{21}\text{Ne}_{\text{cos}}$ production, was slightly less than the chondritic value. There is no
346 suggestion of diffusive loss of ^3He in either sample, in spite of the observation that He
347 degassed at relative low temperature in the laboratory (Table 1).

348 The measured abundances of ^{10}Be for three PAT samples agree within their
349 uncertainties (Table 2). The measured activities of ^{26}Al in four PAT samples (Table 2)
350 span a range of $\sim 17\%$.

351 **4.5 PAT Pre-Atmospheric Size**

352 The $^{22}\text{Ne}/^{21}\text{Ne}$ ratio of ~ 1.09 indicates that the pre-atmospheric shielding
353 experienced by PAT 91501 was somewhat greater than that for typical chondrites. The
354 maximum dimension of the recovered meteorite was ~ 19 cm, which, for the purpose of
355 modeling calculations, sets a minimum radius in space of ~ 10 cm. Modeling of the
356 $^{22}\text{Ne}/^{21}\text{Ne}$ ratio in L-chondrites (Leya et al., 2000) predicts that as the meteoroid radius
357 increases, $^{22}\text{Ne}/^{21}\text{Ne}$ ratios as low as ~ 1.09 are first reached in the center of a body with a
358 pre-atmospheric radius of ~ 30 cm. Thus a somewhat larger body presumably carried the
359 physically separate samples that we analyzed. According to the calculations of both Leya

360 et al. (2000) and Masarik et al. (2001), $^{22}\text{Ne}/^{21}\text{Ne}$ ratios plateau at 1.09 ± 0.01 for pre-
361 atmospheric depths from 10 to ≥ 30 cm in L chondrites with radii of 40 cm.

362 The $^{22}\text{Ne}/^{21}\text{Ne}$ ratio is not useful for setting an upper bound on the pre-
363 atmospheric radius. For this purpose we use the ^{26}Al activity. After a cosmic ray
364 exposure lasting more than 20 My (see below) activities of ^{26}Al (and ^{10}Be) would have
365 reached saturation and are therefore equal to average production rates in space –assuming
366 the terrestrial age of PAT was less than 50 kyr or so as suggested by the normal $^{26}\text{Al}/^{10}\text{Be}$
367 ratios for three samples. According to the calculations of Leya et al. (2000), only
368 meteoroids with radii between 32 cm and 85 cm have the range of ^{26}Al activities
369 observed in PAT. The ^{10}Be activities of PAT 91501 are comparable to those of the L5
370 chondrite St-Robert (Leya et al., 2001), which is thought to have had a pre-atmospheric
371 radius between 40 and 60 cm. We conclude that the pre-atmosphere radius of PAT
372 91501 was in this range.

373 **4.6 Cosmic Ray Exposure Age.**

374 Cosmic Ray Exposure (CRE) ages of stony meteorites were initiated by impacts
375 that reduced meteoroids to objects meter-size or smaller and are almost all < 100 Myr for
376 stones (Herzog, 2005). To calculate cosmic ray exposure ages for PAT (Table 2), we
377 used the cosmogenic production rates for L-chondrites given by Eugster (1988), except
378 that the ^{38}Ar production rate was lowered by 11%, as suggested by Graf and Marti
379 (1995). The production rates were corrected for shielding using the measured $^{22}\text{Ne}/^{21}\text{Ne}$
380 ratios. The differences among ages calculated from He, Ne, and Ar for a given sample
381 are greater than the differences in the same age between the two samples. This pattern
382 suggests that most of the apparent variation in CRE age is produced by our choice of

383 production rates. Because cosmogenic Ar is more sensitive to likely compositional
384 variations and because there is some chance that cosmogenic Ar was incompletely
385 extracted, we give greater weight to the ^3He and ^{21}Ne ages and obtain a CRE age for PAT
386 91501 of 25-29 Myr.

387 We also calculated CRE ages based on the ^{26}Al - ^{21}Ne - $^{22}\text{Ne}/^{21}\text{Ne}$ and ^{10}Be - ^{21}Ne -
388 $^{22}\text{Ne}/^{21}\text{Ne}$ equations of Graf et al. (1990a) by using data for the two samples known to
389 have been adjacent to each other ,34 and ,106. The results, 29.6 Myr and 25.5 Myr,
390 respectively, are in the same range as the CRE ages calculated from the noble gases
391 alone. Finally, we calculated the ^{10}Be - ^{21}Ne CRE age for the ,34 -,106 pair by using the
392 formula of Leya et al. (2000) after modifying it for a ^{10}Be half life of 1.5 My. This age,
393 21.9 My, is about 15-26% lower than the others. Leya et al. (2000) observed that their
394 equation for ^{10}Be - ^{21}Ne CRE ages gives a low result for another large L-chondrite,
395 Knyahinya (preatmospheric radius ~45 cm; Graf et al., 1990b). They attribute the
396 discrepancy to their model's underestimation of ^{10}Be production rates in meteoroids the
397 size of Knyahinya and larger.

398 5. DISCUSSION

399 Among ordinary chondrites, the L chondrites record a particularly severe history
400 of impact bombardment, with almost 5% of this group containing shock melts (La Croix
401 and McCoy, 2007). However, most of these shock features probably occurred during a
402 major disruption of the L-chondrite parent body ~0.47 Gyr ago (Scott, 2002;
403 Korochantseva et al., 2007). Although the old Ar-Ar age for PAT 91501 is atypical
404 among L-chondrites, it is similar to the impact-melted Shaw L chondrite, as was noted
405 during its initial description (Marlow et al., 1992). However, the vesicular nature,

406 presence of preserved, cm-sized metal-troilite intergrowths, and orientation of both the
407 vesicles and metal-sulfide particles in PAT91501 are unusual. These features promise
408 new insights into the timing of and physical processes occurring during the formation of
409 this impact-melted L chondrite.

410 **5.1 Chronology**

411 Chronological evidence for collisional events on asteroids very early in Solar
412 System history is sparse. Among achondrites, some unbrecciated eucrites may have been
413 excavated from depth on Vesta by a large impact ~4.48 Gyr ago (Yamaguchi et al., 2001;
414 Bogard and Garrison, 2003). Chronological evidence for relatively early impacts also
415 exists for parent bodies of the mesosiderites and IIE irons (Scott et al., 2001; Bogard et
416 al., 2000). Within the chondrites, McCoy et al. (1995) reported ages of enstatite
417 chondrite impact melts dating to before 4.3 Gyr and Dixon et al. (2004) suggested that
418 Ar-Ar ages of ~4.27 Gyr for a few LL-chondrites may date the time of one or more
419 impact events on the parent body. Portales Valley is an H6 chondrite, which gives an Ar-
420 Ar age of 4.47 Gyr (Garrison and Bogard, 2001) and contains large metal veins showing
421 Widmanstätten patterns indicative of slow cooling. These phases may have been mixed
422 by an impact (Kring et al., 1999; Haaack et al., 2000). Taken alone, Ar-Ar ages between
423 ~4.38 to ~4.52 Gyr can be ambiguous, as ancient ages may reflect either a late impact or
424 slow cooling after parent body metamorphism (Turner et al., 1978; Pellas & Fiéni, 1988).
425 In contrast, impact melts provide a more direct means for dating the timing of collisional
426 events. Most impact melts give Ar-Ar ages less than 1 Gyr, suggesting that melting and
427 re-solidification took place recently, either during events confined to the surfaces of
428 modern asteroids or, perhaps, when collisions on asteroids melted partially and launched

429 meteoroids into Earth-crossing orbits. This population of more recently formed impact
430 melt rocks includes the vesicular meteorites Cat Mountain (Kring et al., 1996) and Chico
431 (Bogard et al., 1995).

432 In contrast, PAT 91501 dates to the earliest history of the Solar System at 4.461
433 Gyr. Until this work, Shaw was the only ordinary chondrite known to be a near total
434 impact melt (Taylor et al., 1979) and have an Ar-Ar age consistent with an early (>4.0
435 Gyr ago) impact (Turner et al., 1978). Indeed, PAT 91501 shares a number of features
436 with Shaw, particularly its light-colored lithology, petrographic texture and clast-free
437 nature (Taylor et al., 1979). Based on its cosmogenic noble gas concentrations, Shaw has
438 a much younger, nominal one-stage CRE age of ~0.6 My, although in all likelihood,
439 Shaw had a complex exposure history with a first stage that probably lasted >10 Myr
440 (Herzog, 1997). In any event, cosmic-ray exposure ages greater than 1 Gyr are unheard
441 of in stony meteorites and thus Shaw's old Ar/Ar age indicates that the meteoroid did not
442 melt (and hence lose an appreciable fraction of its radiogenic ^{40}Ar) when it was launched
443 from the asteroid. The 4.46 Gyr impact event that formed PAT 91501 apparently took
444 place considerably earlier than those impacts that reset the Ar-Ar ages of Shaw (4.40 ± 0.03
445 and 4.42 ± 0.03 Gyr; Turner et al., 1978). We conclude that PAT 91501 and Shaw formed
446 in different impact events on the L-chondrite parent body, and that the two meteorites
447 were not located in close proximity. There seems little question that PAT 91501 is
448 closely related to the bulk of L chondrites and this relationship is supported by the CRE
449 age for PAT of 25-29 Myr, which lies within a diffuse ~22-30 Myr cluster in the
450 distribution of L-chondrite CRE ages. The 4.46 Gyr impact for PAT 91501 falls within
451 the range of Ar-Ar metamorphic ages of relatively unshocked chondrites (Turner et al.,

452 1978; Pellas & Fiéni, 1988). This observation implies that the L parent body experienced
453 a significant impact while it was still relatively warm. In all likelihood, these events
454 occurred on the original L chondrite parent body prior to any subsequent collisions and
455 breakups that would have formed modern asteroids. These early impacts left PAT 91501
456 deeply buried until it was excavated and launched toward Earth ~28 Myr ago.

457 **5.2 Vesicle Formation**

458 PAT 91501 is remarkable for its mm- to cm-sized vesicles. Vesicles of this size
459 have never before been observed in an impact-melt rock. The few vesicular meteorites
460 that have been investigated in detail are basaltic eucrites or angrites, where vesicles are
461 formed by gases liberated or generated during silicate partial melting (McCoy et al., 2006
462 and references therein). In terrestrial systems, H₂O is the typical vesicle-forming gas, as
463 it is abundant in the Earth's crust and exsolves from basaltic magmas at relatively
464 shallow depths (Oppenheimer, 2004). In contrast, chemical analyses (Jarosewich, 1990)
465 and the presence of abundant Fe,Ni metal suggest that ordinary chondrites likely were
466 very dry systems and, thus, H₂O is unlikely as a major vesicle-forming gas. McCoy et al.
467 (2006) argued that a mixed CO-CO₂ gas was responsible for vesicle formation in
468 asteroidal basalts and the contribution of such a gas cannot be unequivocally eliminated.
469 The contribution of volatiles from the impactor, such as ice in a cometary body, or
470 volatilization of silicates at superheated temperatures also seems unlikely, although
471 impossible to rule out.

472 A much more likely source of volatiles is sulfur vaporization during impact
473 melting. Numerous previous studies have pointed to the role of sulfur vaporization
474 during metamorphic and impact processes of ordinary chondrites. Lauretta et al. (1997)

475 showed that a small amount of sulfur vaporizes at the metamorphic temperatures of
 476 ordinary chondrites. Sulfur vaporization is also a common problem in ordinary chondrite
 477 melting experiments (e.g., Jurewicz et al., 1995) and has been invoked to explain the
 478 formation of sulfide-rich regions in the Smyer H chondrite impact melt breccia (Rubin,
 479 2002). In PAT 91501, the larger vesicles have metal-sulfide intergrowths associated with
 480 them, suggestive of formation by sulfide vaporization during impact melting

481 We can calculate the amount of S gas required to create the abundance of vesicles
 482 (~2 vol.%) documented with computer tomography. The formula for the bulk density β of
 483 a vesicular material is

$$484 \quad 1/\beta = n / \rho_g + (1 - n) / \rho_g \quad (1)$$

485 where ρ_g is the gas density, ρ_g is the density of the non-gas part (i.e. solid or liquid) and n
 486 is the mass fraction of gas. If the conditions are such that the gas law holds at least
 487 approximately, the density of the gas is given by

$$488 \quad \rho_g = (m P) / (R T) \quad (2)$$

489 where m is the molecular weight of the gas, P is its pressure, R is the universal gas
 490 constant (8314 J/kmol) and T is the gas temperature. Substituting for ρ_g :

$$491 \quad 1/\beta = (n R T)/(m P) + (1 - n) / \rho_g \quad (3)$$

492 The two terms on the right are the partial volumes of gas and non-gas, respectively, so the
 493 gas volume fraction v_g is given by

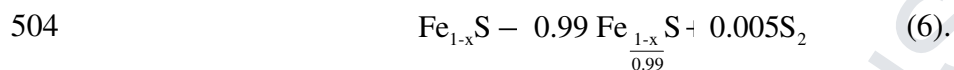
$$494 \quad v_g = [(n R T)/(m P)] / [(n R T)/(m P) + (1 - n) / \rho_g] \quad (4)$$

495 which is more conveniently re-arranged as

$$496 \quad n / (1 - n) = (v_g m P) / [(1 - v_g) \rho_g R T] \quad (5)$$

497 Using the values we estimated, $v_g = 0.02$, $T = 1670$ K, $\rho_g = 3520$ kg m⁻³, $m = 64$ for S₂ or
 498 SO₂, and $P = 5 \times 10^5$ Pa for a depth of a few km in a 50 km radius asteroid, appropriate to
 499 the lithostatic load likely to occur in a silicate melt at depth, we find $[n / (1 - n)] = 1.4 \times$
 500 10^{-5} , so that $n = 1.4 \times 10^{-5}$ to the same precision. If we regard this as the abundance of S₂,
 501 it indicates that ~15 ppm of gas are necessary for formation of the vesicles.

502 Alternatively, we can estimate the amount of S₂ gas produced by vaporization if
 503 all the FeS in a chondrite melted using the following equation from Lauretta et al. (1997):



505 Thus, each mole of sulfide liberates 0.005 moles of S₂. So for a typical L-
 506 chondrite mode of FeS (~4.2vol%), it would be expected that ~210 ppm of S₂ would form
 507 during melting. While this may seem like a small amount, the vesicle volume produced
 508 by this amount of gas would be much greater than that observed in PAT 91501. As we
 509 discuss in the next section, the amount of sulfide present in the impact melt likely results
 510 from gravitational segregation of the dense metal-sulfide particles in the silicate melt. It
 511 is likely that the amount of sulfide that actually vaporized is much closer to about one-
 512 tenth that of average L chondrites, and therefore, a S₂ gas abundance of ~20 ppm is
 513 probably more reasonable, in excellent agreement with above calculations for the amount
 514 of S₂ gas required to create the volume of space occupied by the vesicles.

515 The abundance of 15-20 ppm S₂ required for vesicle formation and in equilibrium
 516 with sulfide is small in comparison to the total mass of sulfur present. Thus, it is no
 517 surprise that evidence for its condensation cannot be found. No sulfide or sulfur linings
 518 have been observed on vesicle walls in PAT 91501, although moderate terrestrial

519 weathering has occurred in the meteorite and hydrated iron oxides of terrestrial origin
520 commonly occur as vesicle linings. We considered the possibility that pentlandite found
521 in the metal-sulfide assemblages might reflect S volatilization. However, no isotopic
522 fractionation consistent with S volatilization was observed between pentlandite and
523 troilite and, as discussed later, it appears more likely that pentlandite is an equilibrium
524 phase formed during cooling in the Fe-Ni-S system.

525 **5.3 Physical Setting and formation of PAT 91501**

526 While PAT 91501 joins a growing list of impact-melted rocks from the L
527 chondrite parent body, its ancient age and large metal-sulfide nodules and vesicles and
528 their striking orientation are unique. Whereas it lacks the abundant unmelted clasts
529 observed in many impact melt breccias, similar clast-poor lithologies are observed in
530 Shaw and, most notably, as a 30 cm wide vein in Chico (Bogard et al., 1995).

531 Mittlefehldt and Lindstrom (2001) suggested that PAT 91501, because of its
532 homogeneously melted nature and relatively slow cooling compared to other impact melts,
533 could be part of an impact melt basal layer found on the floor of a crater (Melosh, 1989)
534 or as a melt dike injected into surrounding country rock (Stöffler et al., 1991). Our work
535 provides additional constraints to distinguish between these two settings. There are
536 several reasons to question the formation of PAT 91501 in a crater floor melt sheet. On
537 Earth, these melt sheets tend to experience rapid cooling and be clast laden. Only in the
538 very largest terrestrial craters (e.g., Manicouagan, Sudbury) where impact melt sheets
539 exceed 200 m in thickness are clast-poor, igneous textured rocks observed (Keil et al.,
540 1997). Likewise, fragmentation of a vesicular lava flow or impact melt sheet will occur
541 at the surface of a low-gravity, atmosphereless body. To achieve the equivalent of

542 terrestrial atmospheric pressure, McCoy et al. (2006) calculated that a melt sheet ~130 m
543 thick would be needed on a body ~250 km in radius. These two estimates are in good
544 agreement and suggest the need for a melt sheet in excess of 100 m thickness. An impact
545 event capable of producing such a thick melt sheet on an asteroid would, instead,
546 collisionally disrupt the body (Keil et al., 1997). Further, floor melts would, at the
547 moment of crater formation, be exposed to space and, thus, the vesicles would degas.
548 Thus, we suggest that a melt dike injected into the surrounding country rock below the
549 impact crater is a more viable setting for the formation of PAT 91501.

550 Injection of molten chondritic material into the surrounding country rock provides
551 both the moderate pressure necessary for vesicle retention and a thermal environment
552 conducive to rapid cooling without quenching. We have been unable to constrain the
553 cooling rate. Although zoning within the large taenite particles might normally be taken
554 as indicative of cooling, we argue instead that the taenite(γ)-troilite-pentlandite
555 assemblage is an equilibrium assemblage formed during cooling at temperatures between
556 ~300-500 °C, consistent with phase relations in the Fe-rich portion of the Fe-Ni-S system
557 (Ma et al., 1998). With the surrounding country rock cooler than the melt, solidification
558 could have occurred in a matter of hours. The absence of distinct clasts in PAT 91501 is
559 not inconsistent with such a model. While most impact melt breccias, by definition,
560 contain unmelted clastic material from the country rock, subcrater melt dikes on Earth
561 exhibit a range of widths (Keil et al., 1997) and it is reasonable to assume that PAT
562 91501 sampled one of the wider, clast-free portions of a dike. Indeed, Bogard et al.
563 (1995) argue that a 30 cm wide zone of clast-poor impact melt in Chico samples such an

564 intrusive dike. At a maximum dimension of ≥ 20 cm, PAT 91501 would not be
 565 extraordinary in this regard.

566 Although cooling and crystallization may have occurred relatively rapidly in this
 567 dike, we suggest that it was far from a quiescent environment. Despite the preservation
 568 of metal and sulfide as mm- to cm-sized nodules, it is clear from the bulk elemental
 569 composition that metal and sulfide were lost from the system. Comparison of metal and
 570 sulfide abundances in PAT 91501 (~0.3 and ~0.5 vol.%, respectively) with those reported
 571 for average L chondrites (3.7 and 4.2 vol.%, respectively; McSween et al., 1991) suggests
 572 that the melt from which PAT 91501 crystallized lost ~90% of the metal and sulfide
 573 component prior to solidification. This loss is not surprising, given the marked density
 574 contrast between molten metal, sulfide and silicate. In fact, a similar density contrast
 575 exists between molten silicates and the vesicles, leading to rapid rise within the melt. The
 576 velocity, u , of settling or rising is determined using the Stoke's velocity equation
 577 (Turcotte and Schubert, 2002)

$$578 \quad u = \frac{1}{3} \frac{\Delta\rho r^2 g}{\eta} \quad (7)$$

579 where $\Delta\rho$ is the difference in density between the metal, sulfide or vesicles and the silicate
 580 melt; r is the radius of the grain of metal or sulfide or vesicle; g is gravity for an assumed
 581 50 km radius parent body (0.012 m/s²); and η is the viscosity of the silicate melt through
 582 which the metal, sulfide or vesicle is moving. We estimated the liquidus temperature of
 583 bulk L-chondrite composition to be between 1400 and 1600 °C, which affects the
 584 viscosity of the melt. Using the maximum size of the metal, sulfide and vesicles

585 determined from the CT scan, we calculate that the largest vesicle would rise at ~3 m/hr
586 while the largest metal particle would sink at ~2 m/hour.

587 One of the most astonishing results from the CT scans is the orientation of the
588 metal/sulfide intergrowths. These orientations, reflected in the relative orientation of
589 metal to sulfide (Fig. 3) and the orientations of metal-sulfide contacts and vesicle
590 elongation – are consistent with formation in a gravitational field. In this respect, PAT
591 91501 is exceptional in that we know which way was up while it was on the asteroid (Fig.
592 3). To the best of our knowledge, only one other meteorite can claim such a distinction.
593 In the Cape York meteorite (Kracher et al., 1977; Buchwald, 1987), elongate troilite
594 inclusions contain chromites concentrated at one end and phosphates at the other, which
595 may be indicative of formation in a gravitational field (Kracher and Kurat, 1975), but
596 have also been attributed to melt migration in a thermal gradient (Buchwald, 1987).

597 In practice, calculated velocities probably represent theoretical maximums, as the
598 vesicles likely coalesced during rise while the metal particles typically contain significant
599 amounts of attached, less-dense sulfide. Nonetheless, these calculations suggest that
600 metal-sulfide particles and vesicles should have rapidly segregated from the volume of
601 melt that eventually crystallized to form PAT 91501.

602 Unless this rock happened to capture a snapshot of metal-sulfide particles sinking
603 and vesicles rising, the retention of any vesicles or metal-sulfide requires another
604 explanation. Far from being dominated by gravitational settling or rising under the
605 influence of buoyancy alone, we suggest that the system was also influenced by the
606 movement of melt within the fracture and the binding of dense metal-sulfide and buoyant
607 vesicles to produce particles of near-neutral buoyancy. When the melt was injected into

608 the cold country rock, it began to rise due to the marked thermal difference, and hence
609 ~10% density difference, between the melt and country rock. Using the method of
610 Wilson and Head (1981), we calculate that the melt rose at a velocity of 0.028 m/s
611 through the dike and solidified due to cooling after migration of ~220 m (McCoy et al.,
612 2006). At this rate, the magma solidified after rising through the dike for ~2 hours.
613 Importantly, the rate of rise of the melt through the dike was roughly an order of
614 magnitude faster than the rate of metal-sulfide settling or vesicle rise. Thus, settling of
615 metal and sulfide to the bottom of the dike was inhibited by the rapid rise of melt through
616 the dike.

617 It also bears noting that the gravitational vector inferred from the metal-sulfide
618 contacts is inconsistent with the orientation of the vesicle long axes (Fig. 4). This slight
619 offset may result from minor turbulence in the rising magma, or possibly an additional
620 lateral component of melt movement that would be reflected in the vesicle shapes but not
621 the gravitational settling of the metal. Alternatively it may reflect the lower solidus
622 temperature of metal/sulfide compared to silicate melt, perhaps permitting time for a
623 vector change between solidifications.

624 Finally, the preservation of metal-sulfide-vesicle assemblages may result from the
625 offsetting differences in density and buoyancy. It is interesting to note that the upward
626 velocities of the average-sized gas bubbles responsible for the vesicles and the downward
627 velocity of the average-sized metal-sulfide grains are very similar at all temperatures. If
628 surface tension forces bind bubbles and grains of comparable size together, offsetting
629 buoyancy may be created that would cause the linked bubbles and sulfide grains to be
630 suspended, or at least to move only very slowly, in the melt. Neutral buoyancy has been

631 suggested for magnetite and vesicles in the Bishop Tuff, where a vesicle either scavenged
632 magnetite crystals from the melt or served as a nucleation point for magnetite growth, in
633 the pre-eruptive magma (Gualda and Anderson, 2007). The attainment of neutral
634 buoyancy in the upward moving melt from which PAT 91501 crystallized might explain
635 the retention of even large metal-sulfide particles.

636

6. CONCLUSIONS

637 Among the abundant impact melt rocks and breccias from the L chondrite parent
638 body, PAT 91501 is unique in exhibiting cm-sized metal-sulfide particles and vesicles,
639 for the remarkable alignment of these particles, and for its ancient age. Sulfur
640 volatilization must have been a ubiquitous process during impact melting of chondritic
641 materials and other meteorites (e.g., Chico) are known that reasonably sample impact
642 melt dikes injected into the crater basement. These other meteorites do not exhibit the
643 large vesicles seen in PAT 91501. This sample must have formed during an early impact
644 on the L chondrite parent body that was large enough to form wide, clast-free melt veins.
645 This process involved relatively slow cooling and crystallization, coalescence and rise of
646 vesicles, coalescence and sinking of metal-sulfide particles, formation of metal-sulfide-
647 vesicle aggregates that were neutrally buoyant, and upward flow of magma in the dike.
648 Although similar processes must have occurred in the formation of other chondritic
649 impact melt rocks, they did not combine in the unique combination that formed PAT
650 91501.

651 *Acknowledgements* – We thank Robbie Score, Cecilia Satterwhite, the Meteorite
652 Processing Laboratory at Johnson Space Center, and the Meteorite Working Group for
653 providing samples. Tim Gooding (Smithsonian) provided expert technical assistance.
654 Larry Nittler and Jianhua Wang provided invaluable assistance with ion microprobe
655 analyses of sulfides and the insights of Joe Goldstein and Jijin Yang helped us understand
656 the formation of zoning within the metal-sulfide particles. We thank Bill Carlson for his

657 early collaboration on the computed tomography aspects of this project and Ralph Harvey
658 and Roy Clarke for their insights into the terrestrial and asteroidal history of PAT
659 91501/91516/91528. Aspects of this work were supported by the NASA
660 Cosmochemistry Program (DDB, TJM, GFH) and the Becker Endowment to the
661 Smithsonian Institution (TJM). Facility support and software development at the
662 University of Texas High-Resolution X-ray CT Facility were provided by NSF grants
663 EAR-0345710 and EAR-0113480. Reviews by Henning Haack, Guy Consolmagno, and
664 Anders Meibom (AE) improved the manuscript and are much appreciated.

REFERENCES

- 665
666
667 Bogard D.D. (1995) Impact ages of meteorites: A synthesis. *Meteoritics* **30**, 244-268.
668 Bogard D.D. and Hirsch W.C. (1980) $^{40}\text{Ar}/^{39}\text{Ar}$ dating, Ar diffusion properties, and
669 cooling rate determinations of severely shocked chondrites. *Geochim. Cosmochim.*
670 *Acta* **44**, 1667-1682.
- 671 Bogard D.D. and Garrison D.H. (2003) ^{39}Ar - ^{40}Ar ages of eucrites and thermal history of
672 asteroid 4 Vesta. *Meteoritics & Planetary Science*, **38**, 669-710
- 673 Bogard D.D., Garrison D.H., Norman M., Scott E.R.D., and Keil K. (1995) ^{39}Ar - ^{40}Ar age
674 and petrology of Chico: Large-scale impact melting on the L chondrite parent body.
675 *Geochim. Cosmochim. Acta* **59**, 1383-1399.
- 676 Bogard D. D., Garrison D. H., and McCoy T. J. (2000) Chronology and petrology of
677 silicates from IIE meteorites: Evidence of a complex parent body evolution.
678 *Geochim. Cosmochim. Acta* **64**, 2133-2154.
- 679 Buchwald V.F. (1987) Thermal migration III: Its occurrence in Cape York and other iron
680 meteorites. *Meteoritics* **22**, 343-344.
- 681 Clarke R.S. Jr. (1994) In *Ant. Meteorite News*. (Score R. and Lindstrom M.M., Eds.) *Ant.*
682 *Meteorite News*. **17**, #1, 15-16. NASA Johnson Space Center, Houston, Texas,
683 USA.
- 684 Dixon, E. T.; Bogard, D. D.; Garrison, D. H.; Rubin, A. E. (2004) ^{39}Ar - ^{40}Ar evidence for
685 early impact events on the LL parent body. *Geochim. Cosmochim. Acta*, **68**, 3779-
686 3790.
- 687 Eberhardt P., Eugster O., Geiss J., and Marti K. (1966) Rare gas measurements in 30
688 stone meteorites. *Naturforsch.* **21A**, 414-426.
- 689 Eugster O. (1988) Cosmic-ray production rates for He-3, Ne-21, Ar-38, Kr-83, and Xe-
690 126 in chondrites based on Kr-81/Kr exposure ages. *Geochim. Cosmochim. Acta*
691 **52**, 1649-1662.
- 692 Garrison D. H. and Bogard D. D. (2001) ^{39}Ar - ^{40}Ar and space exposure ages of the unique
693 Portales Valley H-chondrite. *Lunar Planet. Sci.* **32**, #1137.
- 694 Graf Th. and Marti K. (1995) Collisional records in LL chondrites. *J. Geophys. Res.*
695 *(Planets)* **100**, 21247-21263.
- 696 Graf Th., Signer P., Wieler R., Herpers U., Sarafin R., Vogt S., Fieni Ch., Pellas P.,
697 Bonani G., Suter M., and Wölfli W. (1990a) Cosmogenic nuclides and nuclear
698 tracks in the chondrite Knyahinya. *Geochim. Cosmochim. Acta* **54**, 2511-2520.
- 699 Graf Th., Baur H., and Signer P. (1990b) A model for the production of cosmogenic
700 nuclides in chondrites. *Geochim. Cosmochim. Acta* **54**, 2521-2534.
- 701 Gualda G.A.R. and Anderson A.T. Jr. (2007) Magnetite scavenging and the buoyancy of
702 bubbles in magma. Part 1: Discovery of a pre-eruptive bubble in Bishop rhyolite.
703 *Contrib. Mineral. Petrol.* **153**, 733-742.
- 704 Haack, H., Farinella, P., Scott E.R.D., and Keil, K (1996) Meteoritic, asteroidal, and
705 theoretical constraints on the 500 MA disruption of the L chondrite parent body.
706 *Icarus* **119**, 182-191.
- 707 Haack H., Pedersen T. P., and Rasmussen K. L. (2000) Portales Valley – thermal history
708 of a unique meteorite. *Meteoritics & Planetary Science*, **35**, A67.
- 709 Hartmann W.K., Ryder G., Dones L., and Grinspoon D. (2000) The time-dependent
710 intense bombardment of the primordial Earth/Moon system. In *Origin of the Earth*

- 711 *and Moon* (R.M. Canup and K. Righter, eds.), University of Arizona Press, Tucson,
712 pp 493-512.
- 713 Harvey R.P. and Roedder E. (1994) Melt inclusions in PAT 91501: Evidence from
714 crystallization from an L chondrite impact melt. *Lunar Planet. Sci.* **25**, 513.
- 715 Herzog G.F. (2005) Cosmic-ray exposure ages of meteorites, pp. 347-380. In *Meteorites,*
716 *Comets, and Planets* (ed. A.M. Davis) Vol. 1 *Treatise on Geochemistry* (eds. H.D.
717 Holland and K.K. Turekian), Elsevier-Pergamon, Oxford.
- 718 Herzog G. F., Vogt S., Albrecht A., Xue S., Fink D., Klein J., Middleton R.,
719 Weber H. W., and Schultz L. (1997) Complex exposure histories for meteorites
720 with "short" exposure ages. *Meteoritics*, **32**, 413-422
- 721 Jarosewich, E. (1990) Chemical analyses of meteorites: A compilation of stony and iron
722 meteorite analyses. *Meteoritics* **25**, 323-337.
- 723 Jurewicz A.J.G., Mittlefehldt D.W., and Jones J.H. (1995) Experimental partial melting
724 of the St. Severin (LL) and Lost City (H) chondrites. *Geochim. Cosmochim. Acta*
725 **59**, 391-408.
- 726 Keil K., Stöffler D., Love S.G., and Scott E.R.D. (1997) Constraints on the role of impact
727 heating and melting in asteroids. *Meteoritics and Planet. Sci.* **32**, 349-363.
- 728 Ketcham R. A. (2005) Computational methods for quantitative analysis of three-
729 dimensional features in geological specimens. *Geosphere* **1**(1), 32-41.
- 730 Ketcham R. A. and Carlson W. D. (2001) Acquisition, optimization and interpretation of
731 X-ray computed tomographic imagery: Applications to the geosciences. *Computers*
732 *and Geosciences* **27**, 381-400.
- 733 Koorochantseva E. V., Trieloff M., Lorenz C. A., Buykin A. I., Ivanova M. A., Schwartz
734 W. H., Hopp J., and Jessberger E. K. (2007). L-chondrite asteroid breakup tied to
735 Ordovician meteorite shower by multiple isochron ^{40}Ar - ^{39}Ar dating. *Meteoritics and*
736 *Planet. Sci.* **42**, 113-130.
- 737 Kracher A. and Kurat G. (1975) An unusual phosphate-sulfide assemblage in the Cape
738 York iron meteorite. *Meteoritics* **10**, 429.
- 739 Kracher A., Kurat G., and Buchwald V.F. (1977) Cape York: The extraordinary
740 mineralogy of an ordinary iron meteorite and its implication for the genesis of
741 IIIAB irons. *Geochem. J.* **11**, 207-217.
- 742 Kring D.A., Swindle T.D., Britt D.T., and Grier J.A. (1996) Cat Mountain: A meteoritic
743 sample of an impact-melted asteroid regolith. *J. Geophys. Res.*, **101**, 29,353-29,371.
- 744 Kring D. A., Hill D. H., Gleason J. D., Britt D. T., Consolmago G. J., Farmer M., Wilson
745 S., and Haag R. (1999) Portales Valley: a meteoritic sample of the brecciated and
746 metal-veined floor of an impact crater on an H-chondrite asteroid. *Meteoritics and*
747 *Planet. Sci.* **34**, 663-669.
- 748 La Croix L.M. and McCoy T.J. (2007) Shock Classification of Antarctic Ordinary
749 Chondrites. *Lunar and Planet. Sci. Conf.* **XXXVIII**, abstr# 1601.
- 750 Laurretta D.S., Lodders K., Fegley B., and Kremser D.T. (1997) The origin of sulfide-
751 rimmed metal grains in ordinary chondrites. *Earth and Planet. Sci.* **151**, 289-301.
- 752 Leya I., Lange H.-J., Neumann S., Wieler R., and Michel R. (2000) The production of
753 cosmogenic nuclides in stony meteoroids by galactic cosmic ray particles. *Meteorit.*
754 *Planet. Sci.* **35**, 259-286.
- 755 Leya I., Wieler R., Aggrey K., Herzog G. F., Schnabel C., Metzler K., Hildebrand A. R.,
756 Bouchard M., Jull A. J. T., Andrews H. R., Wang M.-S., Ferko T. E., Lipschutz M.
757 E., Wacker J. F., Neumann S., and Michel R. (2001) Exposure history of the St-

- 758 Robert (H5) fall. *Meteorit. Planet. Sci.* **36**, 1479–1494.
- 759 Ma L., Williams D.B. and Goldstein J.I. (1998) Determination of the Fe-rich portion of
760 the Fe-Ni-S phase diagram. *J. Phase Equilibria* **19**, 299-309.
- 761 Masarik J., Nishiizumi K., and Reedy R. C. (2001) Production rates of ^3He , ^{21}Ne and
762 ^{22}Ne in ordinary chondrites and the lunar surface. *Meteorit. Planet. Sci.* **36**, 643–
763 650.
- 764 Marlow R., Score R. and Mason B. (1992) In *Ant. Meteorite News*. (Score R. and
765 Lindstrom M.M., Eds.) **15**, #2, 30. NASA Johnson Space Center, Houston, Texas,
766 USA 39pp.
- 767 McCoy T.J., Keil K., Bogard D.D., Garrison D.H., Casanova I., Lindstrom M.M.,
768 Brearley A.J., Kehm K., Nichols R.H. Jr. and Hohenberg C.M. (1995) Origin and
769 history of impact-melt rocks of enstatite chondrite parentage. *Geochim.*
770 *Cosmochim. Acta* **52**, 161-175.
- 771 McCoy T.J., Ketcham R.A., Wilson L., Benedix G.K., Wadhwa M., and Davis A.M.
772 (2006) Formation of vesicles in asteroidal basaltic meteorites. *Earth and Planet.*
773 *Sci.* **246**, 102-108.
- 774 McSween H.Y., Bennett M.E., and Jarosewich E. (1991) The mineralogy of ordinary
775 chondrites and implications for asteroid spectrophotometry. *Icarus* **91**, 107-116.
- 776 Melosh H.J. (1989) *Impact Cratering: A Geologic Process*. Oxford Univ. Press, New
777 York, New York, USA. 245pp.
- 778 Mittlefehldt D.W. and Lindstrom M.M. (2001) Petrology and geochemistry of Patuxent
779 Range 91501 and Lewis Cliff 88663. *Meteoritics and Planet. Sci.* **36**, 439-457.
- 780 Middleton R. and Klein J. (1986) A new method for measuring $^{10}\text{Be}/^9\text{Be}$ ratios. *Proc.*
781 *Workshop Tech. Accel. Mass Spectrom.*, (Eds. R.E.M. Hedges and E.T. Hall) June
782 30-July 1, 1986, Oxford, England, 76-81.
- 783 Middleton R., Klein J., Raisbeck G.M. and Yiou F. (1983) Accelerator mass spectrometry
784 with aluminum-26. *Nucl. Instru. Meth. Phys. Res.* **218**, 430-438.
- 785 Oppenheimer C. (2004) Volcanic degassing, in: R. Rudnick (Ed.), *The Crust*, Elsevier-
786 Pergamon, Oxford, pp. 123-166.
- 787 Pellas P. and Fiéni C. (1988) Thermal histories of ordinary chondrite parent asteroids.
788 *Lunar and Planet. Sci. Conf.* **XIX**, 915-916 (abs).
- 789 Rubin A.E. (1985) Impact melt products of chondritic material *Rev. Geophys.* **23**, 277-
790 300
- 791 Rubin A.E. (2002) Smyer H-chondrite impact-melt breccia and evidence for sulfur
792 vaporization. *Geochim. Cosmochim. Acta*, **66**, 699-711.
- 793 Scott, E.R.D. (2002) Meteorite evidence for the accretion and collisional evolution of
794 asteroids, Chapter in *Asteroids III*, W. Bottke, A. Cellino, P. Paolicchoi, and R.
795 Binzel, (eds.), University of Arizona Press, p. 697-709.
- 796 Scott E. R. D., Haack H., and Love S. G. (2001) Formation of mesosiderites by
797 fragmentation and reaccretion of a large differentiated asteroid. *Meteoritics and*
798 *Planet. Sci.* **36**, 869-881.
- 799 Stöffler D., Keil K., and Scott E.R.D. (1991) Shock metamorphism of ordinary
800 chondrites. *Geochim. Cosmochim. Acta* **55**, 3845-3867.
- 801 Taylor G.J., Keil K., Berkley J.L., Lange D.E., Fodor R.V., and Fruland R.M. (1979) The
802 Shaw meteorites: History of a chondrite consisting of impact-melted and
803 metamorphosed lithologies. *Geochim. Cosmochim. Acta.* **43**, 323-337.

- 804 Turcotte D. L. and Schubert G. (2002) *Geodynamics* 2nd Ed. Cambridge Univ. Press,
805 New York, New York, USA 456pp.
- 806 Turner G., Enright M.C., Cadogan P.H. (1978) The early history of chondrite parent
807 bodies inferred from Ar-40-Ar-39 ages. *Proc. 9th Lunar and Planet. Sci. Conf.*,
808 989-1025.
- 809 Vogt S. and Herpers U. (1988) Radiochemical separation techniques for the
810 determination of long-lived radionuclides in meteorites by means of accelerator
811 mass spectrometry. *Fresenius Z. Anal. Chemie* **331**, 186-188.
- 812 Wilson L. and Head J.W. (1981) Ascent and eruption of basaltic magma on the Earth and
813 Moon. *J. Geophys. Res.* **86**, 2971-3001.
- 814 Yamaguchi A., Taylor G. J., Keil K. Floss C., Crozaz G., Nyquist L. E., Bogard D. D.,
815 Garrison D. H., Reese Y. D., Wiesmann H., and Shih C.-Y. (2001) Post-
816 crystallization reheating and partial melting of eucrite EET90020 by impact into the
817 hot crust of asteroid 4Vesta ~4.50 Gyr ago. *Geochim. Cosmochim. Acta*, **65**, 3577-
818 3599.

819
820**Table 1.** Noble gas abundances in two samples of PAT 91501

	³ He 10 ⁻⁷	⁴ He 10 ⁻⁶	²⁰ Ne 10 ⁻⁸	²¹ Ne 10 ⁻⁸	²² Ne 10 ⁻⁸	³⁶ Ar 10 ⁻⁹	³⁸ Ar 10 ⁻⁹	⁴⁰ Ar 10 ⁻⁵
Sample ,109								
500°C	2.33	8.58	0.32	0.30	0.38	0.53	0.47	1.02
1550°C	2.21	36.60	9.12	9.97	10.76	9.42	10.06	2.62
Sample ,106								
500°C	2.70	5.73	0.31	0.029	0.38	0.48	0.48	1.07
900°C	1.68	24.46	3.30	3.56	3.88	1.53	0.87	1.29
1200°C	0.24	0.34	3.24	3.51	3.83	4.50	5.36	0.62
1550°C	0.03	0.12	1.15	1.26	1.37	1.68	2.35	0.17

821

Table 2. Abundances of cosmogenic species and cosmic-ray exposure ages of PAT 91501.

Sample	,106	,109		
³ He	46.5	45.4		
²¹ Ne	8.62	10.27		
³⁸ Ar	0.86	0.99		
²⁰ Ne/ ²² Ne	0.845±0.015	0.847±0.005		
²² Ne/ ²¹ Ne	1.097±0.003	1.084±0.003		
T ₃	28.7	28.0		
T ₂₁	24.6	27.5		
T ₃₈	20.6	23.1		
T ₁₀₋₂₁	29.6			
T ₂₆₋₂₁	25.5			
Sample	,34	,38	,40	,42
¹⁰ Be	20.8	20.6		20.3
²⁶ Al	64.9	61.9	60.6	55.2

Noble gas concentrations in 10⁻⁸ cm³ STP/g. Cosmic-ray exposure ages, T, in Myr. ¹⁰Be and ²⁶Al activities in dpm/kg; uncertainties are estimated to be ±7%. T₁₀₋₂₁ and T₂₆₋₂₁ after Graf et al. (1990a).

822

823

Figure Captions

824 Figure 1. Photograph of PAT 91501 ,50. Numerous vesicles and metal-sulfide grains (up
825 to cm-sized) are visible on the cut surface. Cracks throughout sample are likely due
826 to terrestrial weathering. Scale cube is 1cm on a side.

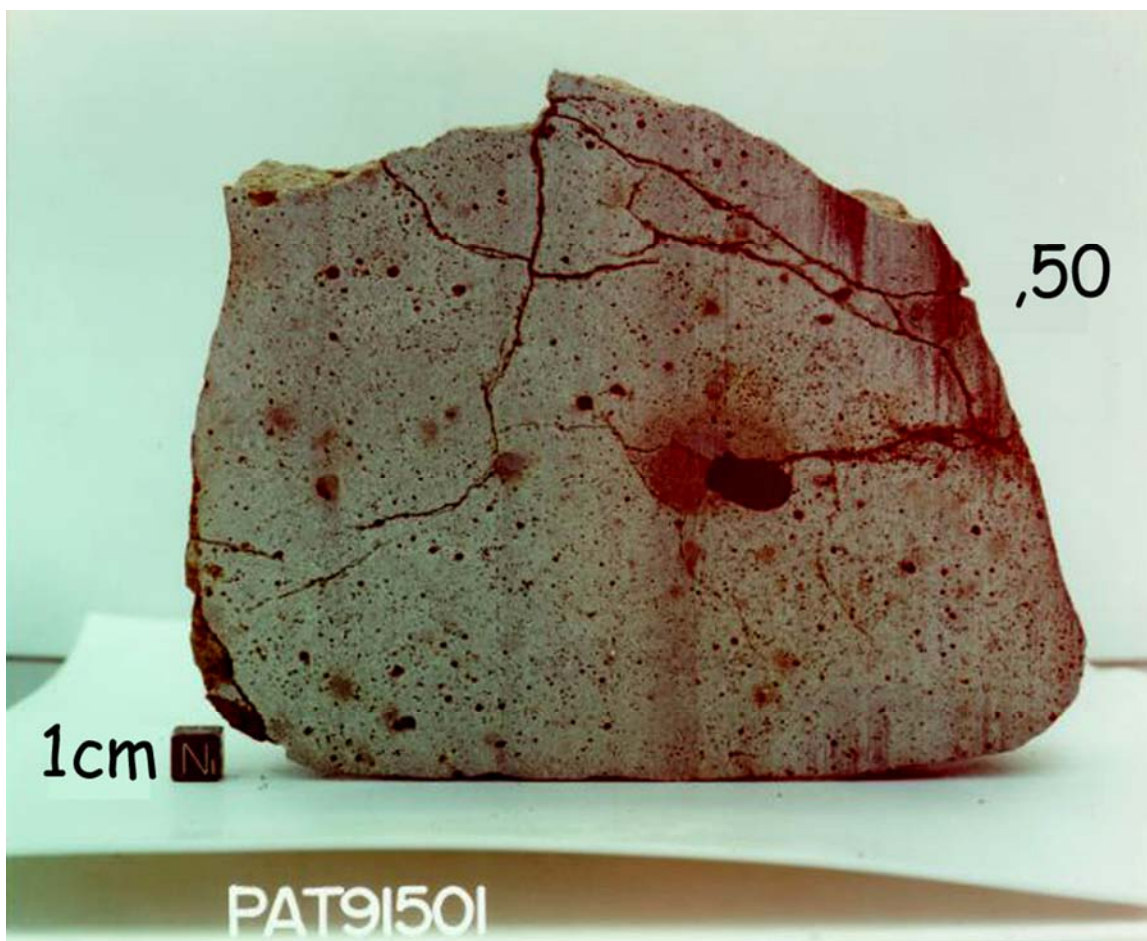
827 Figure 2. A) Reflected light optical photomicrograph of an intergrown metal-sulfide
828 particle in contact with a vesicle in PAT 91501 (,111). The particle has been etched
829 to show the metallographic texture consisting of mainly taenite (t) and martensite
830 (m). Troilite (tr) with small particles of embedded pentlandite (p) rims the entire
831 particle. B) Nickel composition (following traverse illustrated in A) across the two
832 domains showing high-Ni inclusion-free (or poor) taenite rims grading into
833 intermediate-Ni martensitic cores.

834 Figure 3. A single frame from the 3 dimensional rotation visualization made from the CT
835 scan of PAT 91501 (,50), in which vesicles and metal-sulfide intergrowths are
836 highlighted. Metal (yellow), sulfide (magenta) and vesicles (blue bubbles) are set
837 in a semi-transparent outline of the specimen pictured in Figure 1. Arrow points to
838 prominent, large vesicle seen in Fig. 1. The specimen is oriented as it would have
839 been at the time of crystallization as suggested by the metal-sulfide orientations
840 (sulfide above metal in all instances). Note, however, that long axes of vesicles and
841 metal-sulfide masses are offset somewhat to the left.

842 Figure 4. Stereo plots from PAT 91501 (,50) of a) the normals to the planes defined by
843 the contact between metal and sulfide with the size of the each circle proportional
844 to the area of the contact and b) orientations of the vesicle long axes with the circle
845 areas proportional to vesicle volume. Clustering of orientations are observed for

846 both metal-sulfide contacts and vesicle elongation. See text for discussion of
847 orientation directions.

848 Figure 5. Ar-Ar ages (Gyr, rectangles, left scale) and K/Ca ratios (stepped line, right
849 scale) as a function of cumulative release of ^{39}Ar for temperature extractions of a
850 melt sample of PAT 91501. Seven extractions releasing 30-78% of the ^{39}Ar give an
851 age of 4.461 ± 0.008 Gyr, which we interpret to be the formation time of the PAT
852 91501.



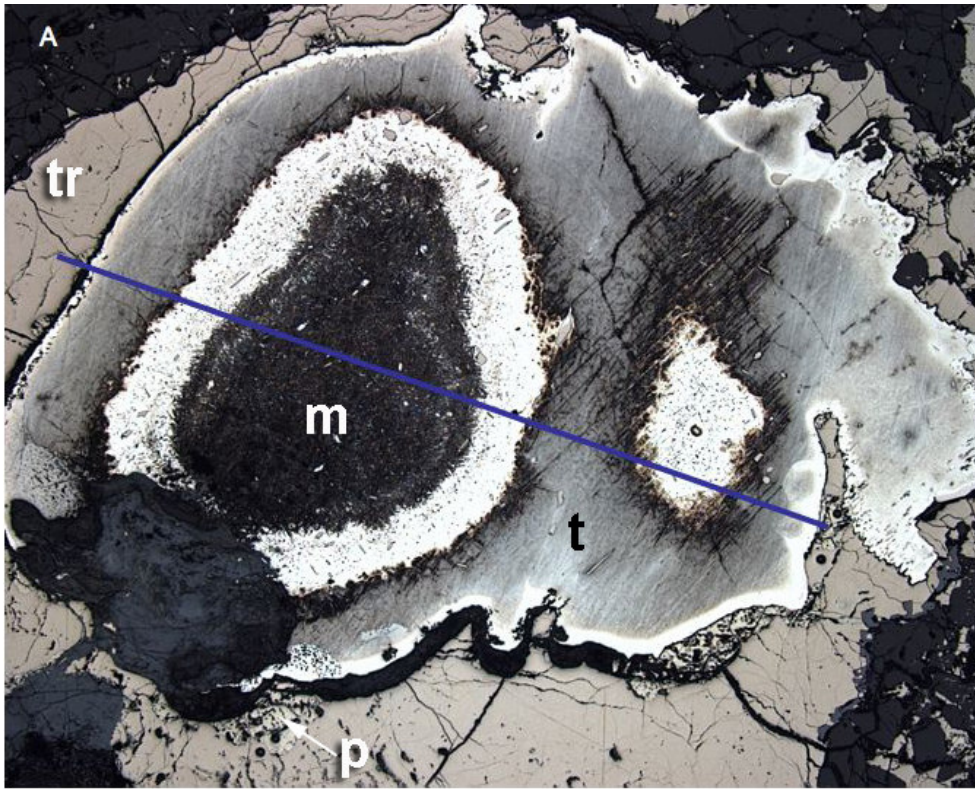
853

854

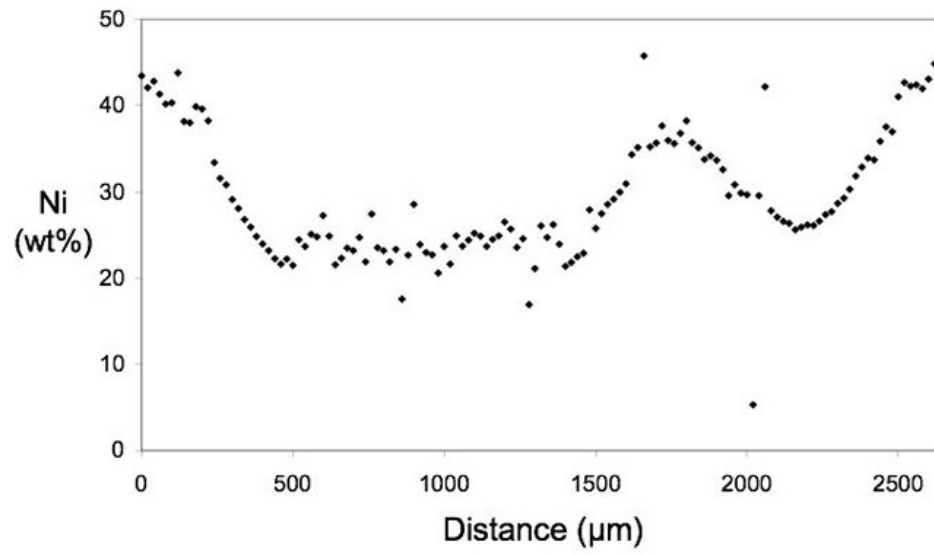
855 Fig.1

856

ACCEPTED

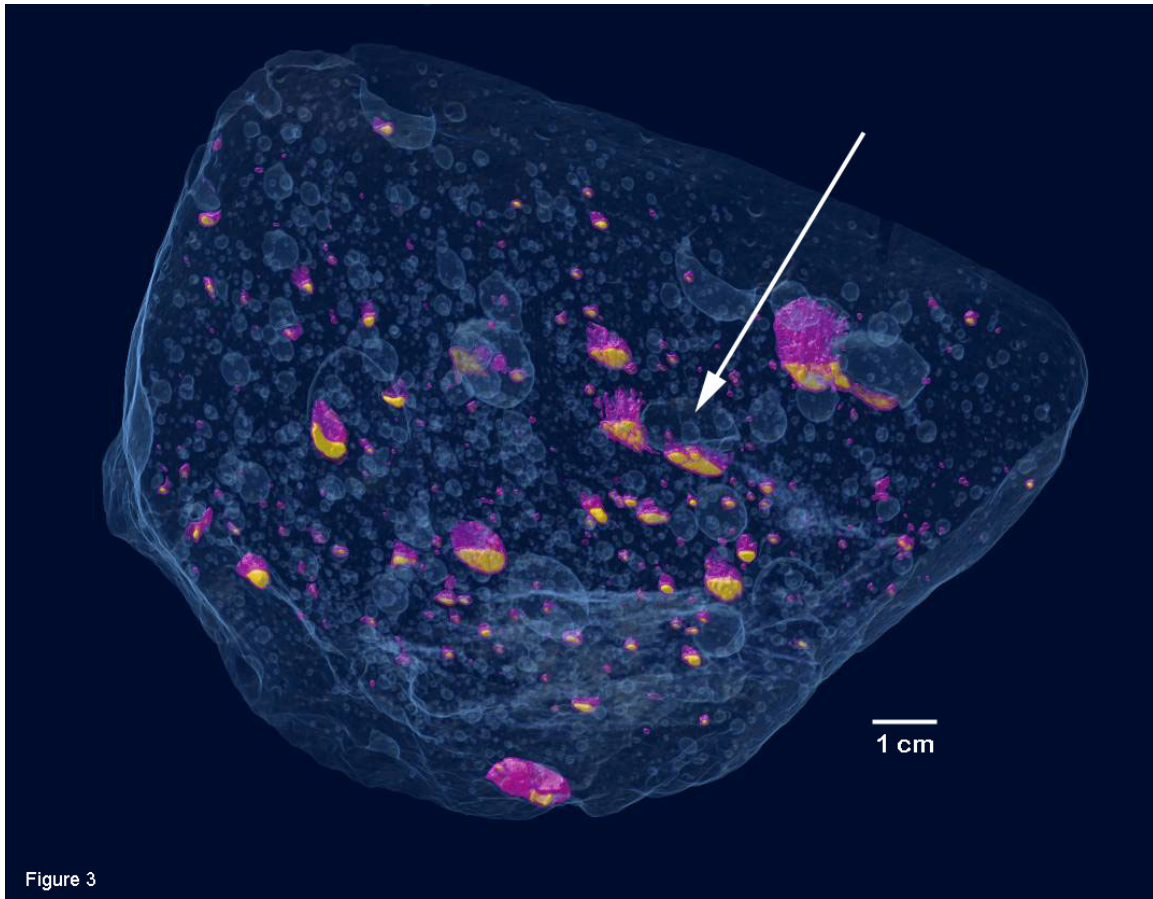


B



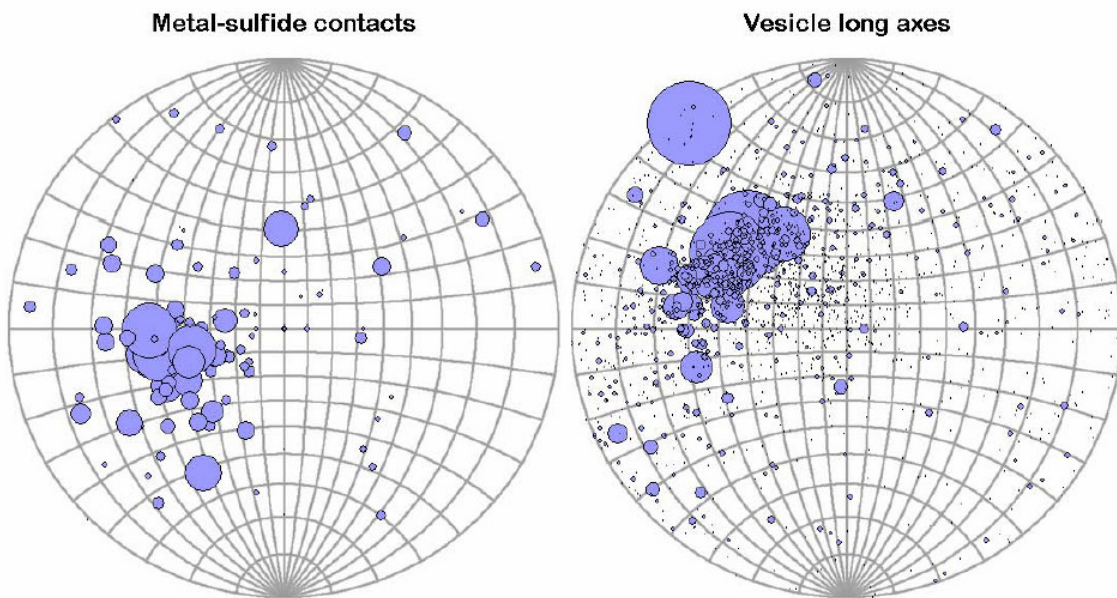
857

858 Fig.2



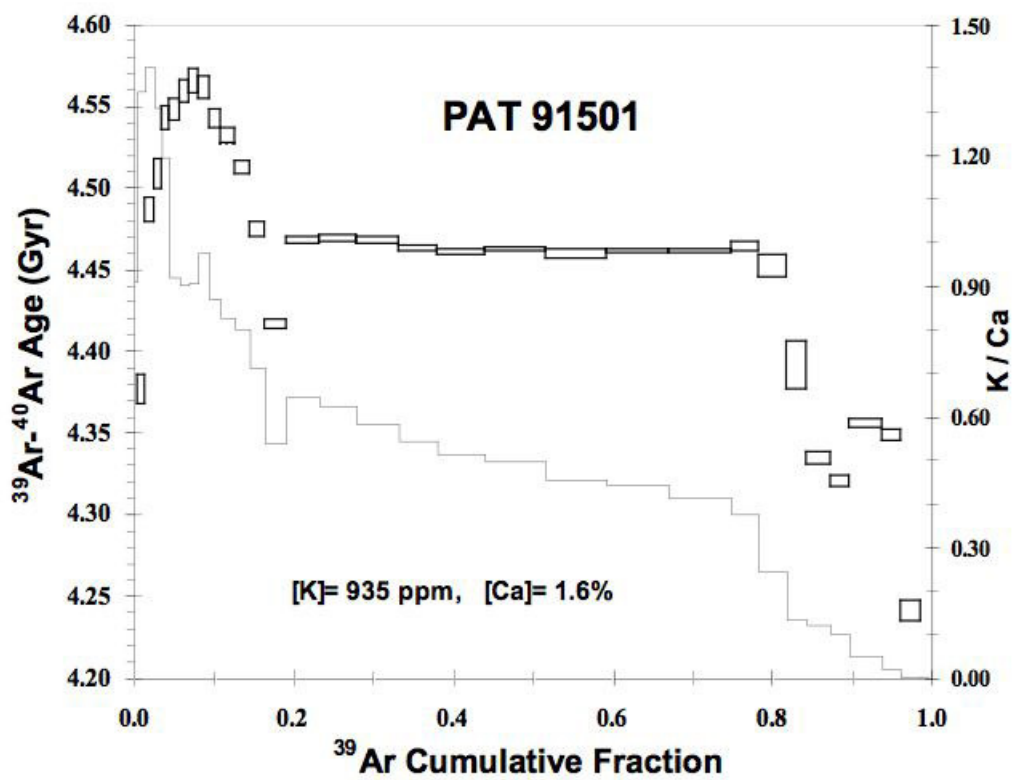
859

860 Fig.3



861

862 Fig.4



863

864 Fig.5

865